Initial Development of the Microcavity Discharge Thruster

IEPC-2009-169

Presented at the 31st International Electric Propulsion Conference,
University of Michigan • Ann Arbor, Michigan • USA
September 20 – 24, 2009

Rodney L. Burton,[1] J. Gary Eden,[2] Sung-Jin Park,[3] Je Kwon Yoon,[4] Mark de Chadenedes,[5] and Steven Garrett[6]
University of Illinois at Urbana-Champaign, Urbana, IL, 61801

Laxminarayan L. Raja[7] and Hariswaran Sitaraman[8]
University of Texas at Austin, Austin, TX,78712

and

Julia Laystrom-Woodard,[9] Gabriel Benavides,[10] and David Carroll[11]
CU Aerospace, Champaign, IL, 61820

Proof-of-concept efforts to demonstrate the propulsion capabilities of microcavity plasma discharges through design and fabrication of a Microcavity Discharge (MCD) thruster are discussed. The primary goal is to design and fabricate a MCD thruster and to demonstrate that the MCD thruster can ultimately achieve performance levels of 1 mN per cavity, a thrust efficiency exceeding 60%, and an I_{sp} of 160 seconds. Because the MCD thruster has low specific mass and is scalable over a large number of cavities, a successful performance demonstration would ultimately result in an advanced propulsion system useful for primary (orbit transfer, maneuvering) and secondary (attitude, position and acceleration control) applications for a wide range of satellites. Research at the University of Illinois (Optical Physics and Engineering, Electric Propulsion labs) and the University of Texas at Austin (Computational Plasma Research Lab) is described. Microcavity electrode arrays with integral micronozzles on each cavity are fabricated and are driven at 20 – 150 kHz at a power level of up to 0.25 W per cavity. Thruster and mass flow measurements are made with cold flow to determine nozzle performance. Heating measurements are made to determine stagnation temperature and heat loss. Computational modeling provides a simulation-based understanding of the plasma physics in the microcavity and supports the experimental measurements. A detailed first-principles computational model provides time-accurate solutions of the multi-species, multi-temperature, self-consistent plasma governing equations for discharge physics, coupled to the compressible Navier-Stokes equations for the bulk fluid flow through the MCD thruster.

---

[1] Professor, Department of Aerospace Engineering, 104 S. Wright St., Urbana, IL 61801
[2] Professor, Department of Electrical and Computer Engineering, 1406 W. Green St., Urbana, IL 61801
[3] Adjunct Associate Professor, Department of Electrical and Computer Engineering
[4] Master's Candidate, Department of Electrical and Computer Engineering
[5] Master's Candidate, Department of Aerospace Engineering
[6] Undergraduate Researcher, Department of Electrical and Computer Engineering
[7] Associate Professor, Department of Aerospace Engineering and Engineering Mechanics, 210 E. 24 St. C0600, Austin, TX 78712
[8] PhD Candidate, Department of Aerospace Engineering and Engineering Mechanics
[9] Senior Engineer, 2100 S. Oak St., Suite 6, Champaign, IL, 61820
[10] Senior Engineer
[11] Vice President

Nomenclature

A^* = nozzle throat area, m^2
C_d = discharge coefficient
C_p = isobaric specific heat, J/(kg K)
C_f = thrust coefficient
$F(\gamma)$ = algebraic function of gamma for choked flow
g = gravitational acceleration, m/s2
$\dot{m}$ = mass flow rate, kg/s
p_o = stagnation pressure, Pa
Re = Reynolds number
T = thrust, N
T_o = stagnation temperature, K

I. Introduction

ONE of the most complex issues that remains to be dealt with in order for wide adoption of micro-, nano-, and picosatellites systems is the lack of a simple, efficient, and most importantly highly compact propulsion system for primary (orbital transfer and maneuvering) and secondary (attitude and trajectory control) thruster applications. Recent advances at the University of Illinois in using microcavity plasma discharges for illumination[1, 2] have provided a possible solution to this problem in the form of a Microcavity Discharge (MCD) thruster. The MCD thruster constitutes a new type of advanced electrothermal thruster consisting of a gaseous propellant supply, two insulated Al/Al_2O_3 electrodes powered by a 50-150 kHz, 400-1200 V AC supply, a 70-130 μm diameter cavity which confines the discharge plasma, and an integral moderate Reynolds number micronozzle to increase thrust.

The heart of the thruster is the technology breakthrough of the MEMs-scale plasma discharge, the properties of which are highly adaptable to propulsion. Over the past decade, it has been found that low temperature plasma confined to a microcavity has several remarkable properties, including specific power loadings (i.e., volumetric power deposition into the plasma) of up to ~100-1000 W/mm^3 on a steady state basis (~2 MW/mm^3 have been realized in a pulsed mode), operating pressures of < 100 Torr to above one atmosphere, and electron temperatures of 4-6 eV and higher. This region of parameter space has not previously been accessible to plasma science but it is already clear that these parameters open entirely new avenues for applications of plasma technology.

By leveraging microfabrication techniques developed largely by the VLSI and MEMs communities, researchers at the University of Illinois (Urbana-Champaign) have successfully fabricated and operated microcavity plasma devices with cavities having characteristic dimensions as small as 10 μm. Furthermore, arrays comprising as many as 10^6 microplasmas have now been realized. This effort has been supported by numerical modeling of the microdischarges[3], to better understand the dominant physical mechanisms. This paper presents initial experimental and computational results for this new propulsion concept.

Accordingly our basis for adapting MCD technology to a thruster is the expected system benefits of high specific thrust, high thrust density, and high specific power, with high propellant utilization and a simple power processor. For very small scale electrothermal thrusters gas heating to temperatures of >1000 K is only possible with microdischarges. Other concepts such as microresistojets can achieve gas heating of only a few 100 K above ambient because of limitations in the MEMS resistive heating elements. Most importantly the microdischarge gas temperature can be tuned to range from ambient values to high values by changing the power input. The overall thruster efficiency is predicted to be greater than 60%, and power scalability is straightforward over a wide range. Additionally, the service lifetime of the thruster is expected to be long due to the lack of electrode sheaths and the capability of operating without an auxiliary neutralizer.

Electrothermal microdischarge propulsion systems are low power, high thrust density devices, sometimes referred to as advanced electrothermal devices, operating at the lower end of the specific impulse range. They are predicted to show significant I_{sp} improvement over cold gas systems, but cannot compete for I_{sp} with Hall thrusters for 500 – 3000 kg satellites in the 0.5 – 3 kW range. However, they can compete in power-limited situations and can be used for ACS, position control and acceleration control on these satellites, either using xenon or a lower molecular weight propellant (including liquid ammonia vapor), depending on mission requirements. The microdischarge power processing unit is extremely simple, compact and efficient, consisting only of a low voltage DC-AC converter with >95% efficiency and a specific mass of ~ 3 g/W. Propellant utilization is very high, and ion cost is very small for high pressure microdischarges with ion fractions well below 0.01%. They also have an

extremely low mass and volume footprint. For flight hardware, MCD thruster systems can provide a significant improvement in terms of thruster specific weight (kg/W) and specific volume (cm^3/W). Microdischarge systems are expected to be relatively easy to integrate onto spacecraft, and early versions could be flight-tested at low cost in the near future using 1-3 kg CubeSats. (The University of Illinois 3 kg standard CubeSat bus can support a 1.5 kg, 3 W propulsion system as a payload, more than enough for a microdischarge system and a significant amount of propellant.)

Microdischarge arrays can be scaled in power from 100s of milliwatts up to kilowatt levels. Thrust is available at all power levels, including zero power, and they present minimal additional system complexity. An important aspect is the scalability from very small to significantly large thrusters, as virtually any desired number of cavities can be run in parallel, with equally high efficiency. Unlike normal glow or arc discharges that have a negative resistance V-I characteristic and are thermally unstable in parallel without ballast, the microdischarges operate in the abnormal glow mode, with ionization fraction <<1% and a positive V-I characteristic, thus allowing parallel operation and power scaling. Figure 1 displays the positive slope of the V-I curve, which is discontinuous at a breakdown voltage characteristic of the gas, in this case neon.

As much as 2 W per cavity has been demonstrated, with a plasma temperature of 1500 K, achieved with aluminum electrodes encapsulated in Al_2O_3. Despite this high temperature, no damage is observed to the electrode structure over hundreds of hours.

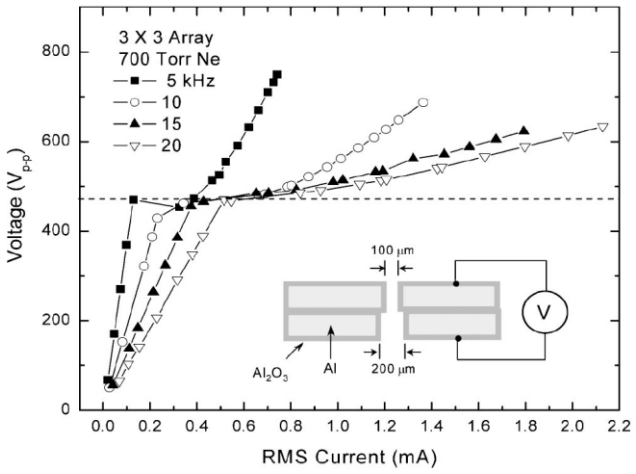

Figure 1.[2] Voltage-current (V-I) characteristics for a 3 x 3 cavity array of Al_2O_3/Al micro-discharge device, qualitatively illustrated in the inset.

The MCD thruster builds on, but also represents a significant departure from, previous microthruster efforts. The microthruster work by Bayt[4] contains valuable data on micronozzle performance with nitrogen at Reynolds numbers from 380 to 3700. Cold thrust efficiencies exceeding 88% were achieved for Re>300. Attempts at heating the thruster propellant with a micro-heat exchanger allowed a total temperature of 700 C to be reached, although heat losses through the power leads reduced the thrust efficiency to ~20%.

The resistojet concept, which uses hot metal surfaces to heat propellant, goes back to the 1950s, and was one of the earliest types of electric thrusters developed[5]. The principle resistojet loss is heat loss through the insulation,[6] although efficient nozzle performance was demonstrated at low Reynolds numbers.

The question of thrust production with micronozzles was also investigated for a pulsed arcjet, and showed not only efficient nozzle performance, but also high thrust efficiency[7,8] with a pulsed discharge, operating similarly to the MCD thruster. The pulsed arcjet is a 2500 Hz, capacitor-driven arc discharge in a 2.5 mm diameter dielectric capillary coupled to a 380 μm diameter nozzle, with best performance achieved with a nozzle area ratio of only 4:1. For helium at 32 W, the device achieved 57% efficiency and thrust of 23 mN at I_{sp} = 231 s. The overall efficiency was encouraging considering the large wall area of the capillary tube and the pulsed discharge and resulting flow field in the thruster.

Another design is the Japanese microwave microthruster[9] (MMT), which uses argon at 5 – 10 W, heated by microwaves in a 9.5 mm long by 0.96 mm diameter dielectric cavity. Thrust efficiency is less than 10% with a nozzle, primarily because the wall area is relatively large compared to the throat area. For the MMT, A_{wall} = 64 mm^2, vs. 0.05 mm^2 per cavity for the MCD thruster. With a comparable wall ΔT and microwave dissipation, the fractional wall heat loss approaches 75%.

The Micro-discharge micro-thruster[10] most closely resembles the MCD thruster. Low pressure argon gas (~ 3 kPa) passes through a choked 300 μm orificed electrode, expands supersonically for 1500 μm through a boron nitride nozzle, and passes through a second orificed electrode with diameter as large as 2500 μm, into high vacuum. This device is distinguished from the MCD thruster in that the discharge pressure is three orders of magnitude smaller, the discharge is DC rather than AC, and the electrodes are directly coupled to the plasma. The device demonstrates significant plasma ionization, and with the low particle collision frequency results in a large frozen

flow loss and low exhaust kinetic energy. The MCD thruster avoids these problems by operating at high pressure, typically ~100 kPa, and locating the discharge in the subsonic flow upstream of the throat.

Our past experience with other microthrusters[7,8,11] has shown that the dominant flow loss is the nozzle frozen flow loss due to dissociation and ionization. For the MCD thruster neon frozen flow losses are not a concern, since monatomic neon has a very small degree of ionization (10^{-3} – 10^{-5}). It is instead likely that a major determiner of thrust efficiency is viscous losses in the nozzle due to the required Reynolds number regime.

To briefly summarize, the MCD thruster has a number of advantages, including:

1. Discharge power densities of 100-1000 W/mm^3
2. Low wall heat loss due to a wall area on the order of 0.05 mm^2 per cavity
3. Operating temperature of over 1000 K. Temperatures of 1500 K have been observed and temperatures of 2000 K are possible.
4. Ionization fraction << 1% and small resulting frozen flow losses
5. No auxiliary systems, e.g. neutralizer, heater or igniter are needed
6. Operating pressures are approximately 1 atm, giving nozzle Reynolds numbers of several hundred, and acceptable viscous losses
7. Power processing is accomplished with a DC-AC converter with low mass, and with PPU efficiency exceeding 95%
8. No exposed electrodes (capacitive discharge coupling), eliminating electrode sheath drop
9. Very low system mass and volume for use on very small (<10 kg) satellites

II. Experimental Approach

A. Electrode Configuration

Figure 2 shows the basic MCD concept. Aluminum foil electrodes, containing a number of cavities from one (shown) up to 10^6, are fabricated in pairs. A layer of Al_2O_3 is then grown on the foil in a process called nanoporous structure anodization. The foils are combined and a nozzle shape is chemically etched (Fig. 3). The foil assembly is then bonded to a feedtube connected to the gas supply. For the heating tests, the electrodes were fabricated with both electrodes located upstream of the throat, so as to cause the discharge heating to occur in the subsonic region of the flow.

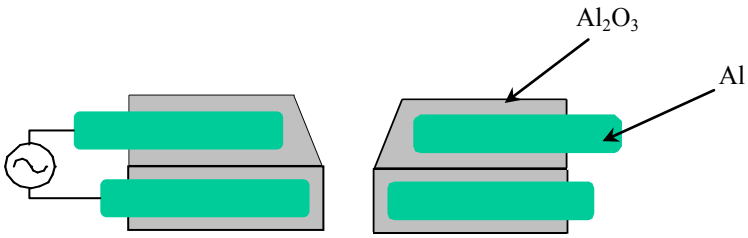

Figure 2. Schematic of insulated electrode pair and microcavity with integrated micronozzle. Typical nozzle throat diameter is 100 μm.

B. Micronozzle Fabrication

The Illinois Laboratory for Optical Physics and Engineering has demonstrated the ability to control the cavity cross-section (Figs. 3 and 4), required for the micronozzle[12,13]. Precise control of the cross-sectional geometry and surface morphology of the cavities within Al/Al_2O_3 microplasma devices having a dielectric barrier structure has been achieved with a sequence of wet electrochemical processes. This process can be used to provide the micronozzle profile. The micronozzle diameters tested to date in this program are 75-100 μm throat and 100 - 210 μm exit diameter.

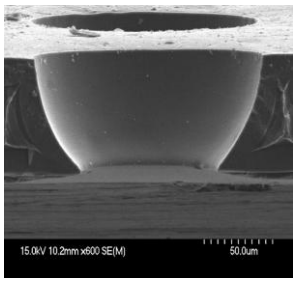

Figure 3. Univ. of Illinois Al_2O_3 micro-machined bell nozzle for MCDT.

Continuous variation of the cavity cross-section between a linear taper and parabolic geometry can be specified and all dimensions controlled to within ± 2%. Control of the micronozzle profile by a sequence of wet chemical processes permits the optimization of both the electric field variation within the cavity and the flow expansion efficiency. Figure 4 illustrates several of the microcavity cross-sectional geometries that can now be realized, from linear to parabolic. We expect this result will significantly improve the efficiency of the microthruster.

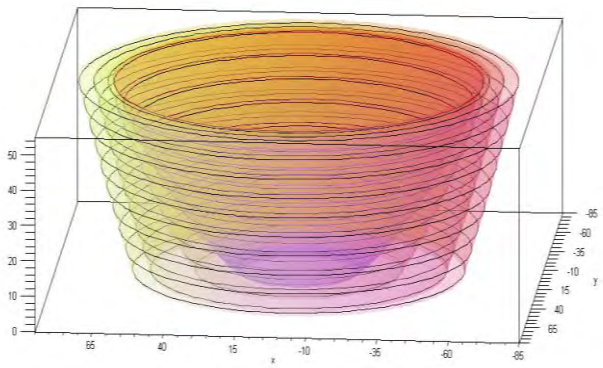

Figure 4. Simulation of "bowl-shaped" microcavities fabricated by wet chemical processing of Al foil. The curvature of the microcavity can be precisely determined to within ± 2% by controlling the time and current of a modified anodization process.

C. Experimental Procedure

For discharge testing, ultra high purity grade (99.999% pure) gaseous neon and nitrogen propellant gases are supplied to gas feedlines by regulated high pressure tanks. The gas flows are measured by two Omega Engineering mass flow sensors, a FMA3104 series, 200 mL/min capacity sensor for the nitrogen and a FMA3105 series, 500 mL/min capacity sensor for the neon, both with air as the calibration gas. Each gas feed line passes through a Swagelok SS-SS4 choked metering valve for precise flow control. The gasses are mixed downstream of the metering valves and the mixture pressure is measured by a Cole-Parmer 68072-52, 0-50 psia range pressure transducer connected to LabVIEW through a National Instruments Data Acquisition (NI DAQ) card. Once mixed, the gases are fed to the microcavity assembly.

The microcavity is contained within a vacuum chamber to establish choked flow, simulate space conditions, and to evacuate discharge gases to prevent external discharge or arcing. The vacuum tank has a number of ports through which the mixed propellant gasses are fed, and the current probe, voltage probe, and power lines are run. The vacuum is created and maintained by an Alcatel 2012A rotary vane pump and a Varian Turbo-70D 969-9361 series turbopump running in series. Typical vacuum pressures during testing are on the order of 15-100 mTorr. A tested thruster is shown in Fig. 5.

Power is supplied to the MCD thruster by means of a three stage supply. A Wavetek Model 164 30 MHz Sweep generator (which will be replaced by a newer generator in future testing) provides a sinusoidal waveform to a Mackie FR 800 two-channel 800 Watt amplifier. The amplified signal is then run through a custom-built 100:1 step-up transformer and then to the electrodes. The system has delivered frequencies up to 150 kHz and voltages as high as 1.2 kV.

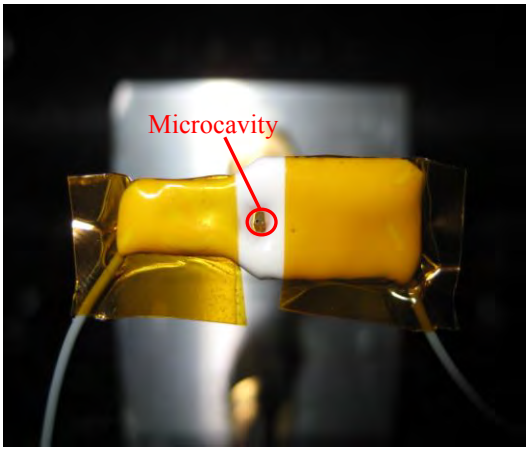

Figure 5. Test version of 120 μm microcavity discharge (without micronozzle) used for neon flow heating.

The power input to the electrode during discharge was measured with a Tektronix TDS 3034B 4-channel oscilloscope using a Tektronix P6015 1000x high voltage probe and a Pearson 4100 current monitor. The instantaneous voltage and current readings are multiplied and summed over the points contained in one period and then divided by the number of points in a period to determine the power. The voltage, current, frequency, and power readings are displayed on LabVIEW for data recording and analysis.

The cold thrust of the MCD thruster is measured using the UIUC compact thrust stand,[14] which is capable of determining the generated thrust with an accuracy of ± 0.05 μN. To calibrate the thrust, calibration weights with a known mass are lowered by a pulley from the edge of the thrust stand thus displacing the platform. When the thruster operates, it also displaces the platform. Thrust stand deflection is measured with a Schaevitz linear variable differential transformer (LVDT) with a sensitivity of 7.71 V/mm and an accuracy of +/- 1 μm. The unknown thrust is then determined using the known calibration curve and the measured displacement. For these tests, the period of the horizontal thrust stand oscillations was set at ~ 5 seconds. A propellant supply feedline, whose stiffness varies with pressure, runs vertically from the roof of the tank to the platform. Calibrations are taken as a function of feedline pressure: 120, 180, and 240 kPa (Fig. 6).

The electrode used for the thrust measurements has four parallel cavities with 120 μm throat diameter and a diverging bell nozzle having 210 μm exit diameter. The nozzle profile is similar to that shown in Fig. 3. This particular bell nozzle is not optimum, because the turning angle from the duct into the nozzle is too large, about 70 degrees, a value achieved by an early fabrication attempt. Future nozzles will use reduced turning angles of ~30 degrees.

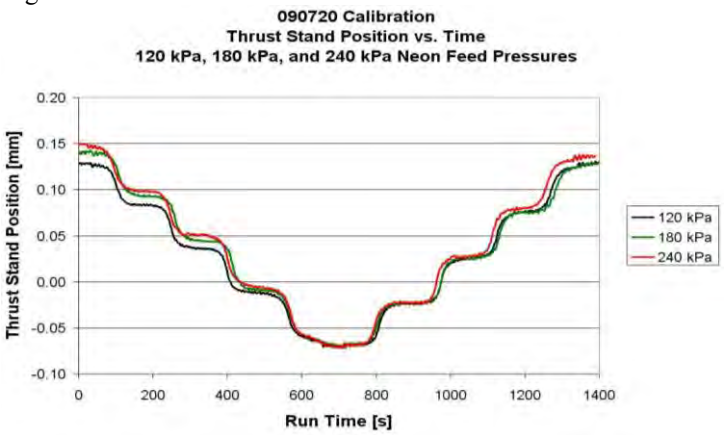

Figure 6. Thrust calibration data vs. absolute neon feed pressure. Each weight adds 0.34 mN horizontal force to the stand, giving a deflection constant of ~0.15 mm/mN depending on pressure.

III. Experimental Results

A. Flow Tests

It was determined early in testing that a flow of pure neon would absorb insufficient power to provide significant heating. Therefore, small percentages of polyatomic gases (N_2, H_2O) were added to the neon, which dramatically increased power absorption. Initial flow test results are shown in Table 1, for neon with 2.7% added N_2 mass flow. The flow total temperature T_0 is inferred from the measured mass flow rate, pressure p_0, discharge coefficient C_d, flow area A^* and known specific heat ratio γ, according to:

$$\dot{m} = \frac{F(\gamma) p_o C_d A^*}{\sqrt{T_o}}$$

Heating the flow upstream of the exit throat, as is done here, raises T_0, so that the cold and hot T_0 can be determined from the flow measurements. Table 1 shows a flow heating efficiency of 88%, implying a relatively small fraction lost to the walls.

Table 1. Flow heating of single cavity, Ne + 2.7% N_2 @ 50 kHz.

Discharge diameter, μm	110
Discharge power P, mW	135
Total flow rate, mg/s	1.29
Discharge coefficient	0.89
Temp rise ΔT_0 from flow rate, K	90
Flow heating $Q = \dot{m} C_p \Delta T$, mW	119
Heating efficiency, Q/P	119/135 = 0.88

B. Microdischarge Tests

Cavity power can be increased by several methods. The most direct method is by increasing the discharge voltage, which raises both voltage and current (Fig. 7). Figure 7 shows the relationship between input power and voltage at a frequency of 50 kHz for a 110 micron throat diameter single cavity electrode using pure neon propellant. It can be seen that the input power rises proportionally to the electrode peak-to-peak voltage, giving another method for controlling the electrode power in addition to frequency adjustment. An important element of this figure is the slope of the best fit line which is not one-to-one, indicating a current trade off for a voltage increase. A second method (Fig. 8) is to increase the frequency of the input power. Figure 8 shows the relationship between the measured input power and frequency (30 – 150 kHz) for a 110 micron throat diameter single cavity electrode using pure neon propellant. For a given discharge pressure there appears to be a direct linear correlation between the frequency and input power. In general a higher frequency will produce a greater input power, a finding

supported by the computational model. Lastly, the power can also be increased by adding polyatomic species to the gas mixture. We have measured cavity power levels as high as 250 mW with a combination of these techniques.

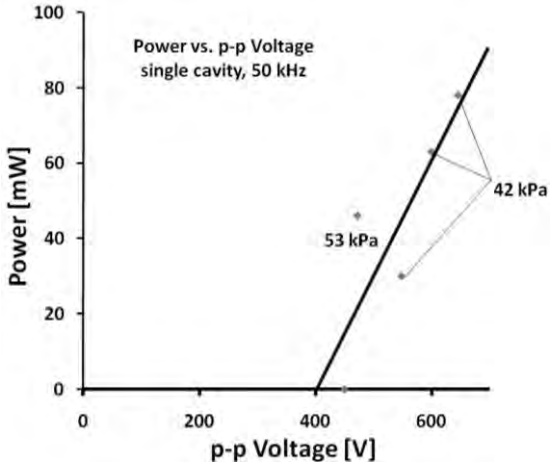

Figure 7. Power versus peak-to-peak voltage above breakdown using pure neon propellant.

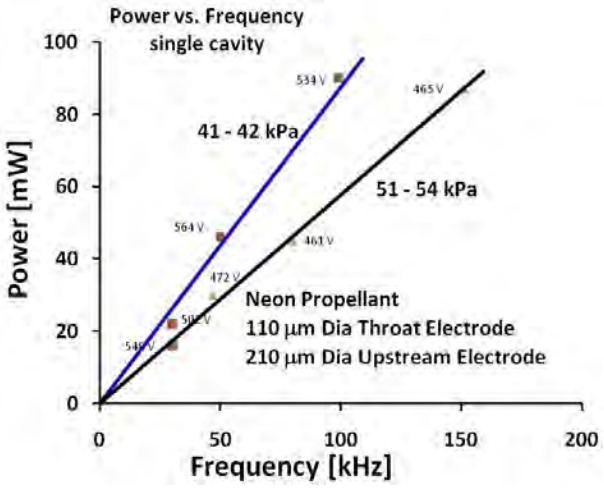

Figure 8. Absorbed power vs. discharge frequency at two pressure levels, showing linearity using pure neon propellant.

C. Thrust Stand Nozzle Tests

The electrode used for the cold gas thrust measurements had four 120 µm throat diameter cavities, each with a diverging bell nozzle having 210 µm exit diameter. The bell nozzles had non-optimum turning angles from the duct into the nozzle of approximately 70 degrees. Future nozzles will use turning angles of 20-30 degrees.

Table 2 and Eq. 1 show the calculations and results for 240 kPa neon feed pressure and throat Reynolds numbers of 600 and 1900. Thrust results are shown in Fig. 9. It is desirable to raise Re by reducing the throat diameter.

Table 2. Neon thrust and thrust coefficient, 4 cavity array.

Neon Line Pressure [kPa, abs]	Mass Flow Rate [mg/s]	Thrust [mN]	Reynolds Number	C_f (one cavity)
120	0.99	0.60	600	1.26
240	5.22	2.70	1900	1.07

where thrust coefficient is defined as:

$$C_f = \frac{T}{p_o g A^*} \qquad \text{(Eq. 1)}$$

These values of thrust coefficient are comparable to thrust coefficients measured by Bayt[4] in a MEMs thruster with a 37 µm throat.

D. Spectroscopic Temperature Measurements

A preliminary temperature measurement was performed spectroscopically on a device with two electrodes and total device thickness of ~350 µm. These small discharge gaps reduce the ignition voltage significantly, and ignition voltage in Ne gas flow is found to be

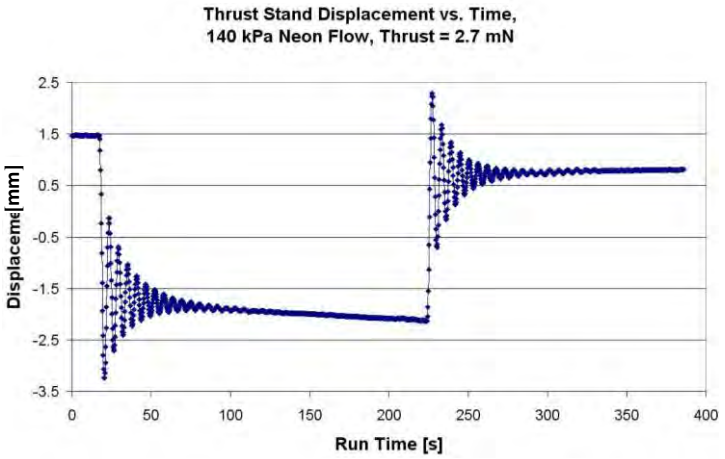

Figure 9. Thrust stand displacement vs. time.

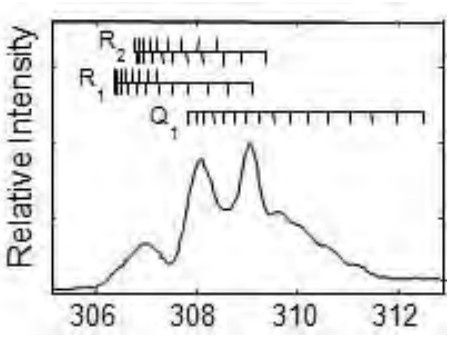

Figure 10. A → X transition from the emission spectrum of microplasma in Ar/H_2O gas mixtures.

250 - 300 RMS V with a sinusoidal excitation waveform. The applied ac frequencies are proportional to the power loading, and ranges of 25-100 kHz were used for the test. To measure temperature, a small fraction of N_2 or H_2O was added to a Ne or He flow, which also increases the power dissipation inside the microcavity. According to the rotational-vibrational spectroscopy of microplasmas in these gas mixtures (especially A → X transition from a discharge of noble gas and H_2O mixture, Fig. 10), the gas temperature is measured to be higher than ~ 500 K in a no-flow condition.

IV. Computational Modeling of the Microcavity Discharge

The flow and plasma phenomena in the micro cavity discharge thruster are strongly coupled. The flow modifies the number density, velocity and pressure of the background species which affects the plasma. The plasma in turn causes gas heating which affects the flow.

The plasma governing equations[15] are solved along with the bulk flow compressible Navier-Stokes equations on an Unstructured Finite Volume framework. The plasma governing equations are based on a multi-species multi-temperature continuum model along with Electrostatic Poisson Equation to calculate the electric field. The model also uses finite rate neon nitrogen (97% Ne, 3% N_2) chemistry which will be described below. The rate coefficients for the electron collision reactions depend on the electron temperature which is obtained from the electron temperature equation. The continuum approach used here is reasonably valid at the current operating pressures (1-130 kPa) and characteristic dimensions (on the order of 100 μm). The transport properties of charged species are assumed to be dependent only on collisions with the dominant neutral species. The heavy species are assumed to have a common gas temperature which is reasonable because of a very small energy transfer mean free path during their collisions with each other.

A. Plasma Governing Equations

1. Species Continuity

The number densities of each species which includes ions, metastables and electrons are solved using the species continuity equation given below.

$$\frac{\partial n_k}{\partial t} + \vec{\nabla}\cdot\vec{f}_k = G_k\frac{\partial n_k}{\partial t} + \vec{\nabla}.\vec{f}_k = \dot{G}_k \quad , \quad \text{k} = 1\ldots\text{K}_\text{g} \quad \text{(k is not background species)}$$

Here n_k is the number density of species k, $\vec{f}_k\,\vec{f}_k$ is the particle flux of species k which includes the bulk velocity also and $G_k\dot{G}_k$ is the production of species k through chemical reactions. The densities of background neutral species are obtained from the ideal gas law.

$$P = n_{k_b}k_BT_g + n_ek_BT_e + \sum_{k\neq k_e, k\neq k_b} n_kk_BT_g$$

Here P represents the local pressure, $n_{k_b}\,n_{kb}$ represents the neutral gas number density, n_e and T_e represent number density of electrons and electron temperature and k_B is Boltzmann's Constant.

The flux term $\vec{f}_k\,\vec{f}_k$ is given by the drift diffusion approximation

$$\vec{f}_k \equiv n_k\vec{u}_k = -\mu_kn_k\vec{\nabla}\phi - D_k\vec{\nabla}n_k + n_k\vec{V}_k$$

Here ϕ is the electrostatic potential $\mu_k\,\mu_k$ is the mobility of species k, D_k is the diffusion coefficient, and V_k is the convective velocity.

2. Electron Energy

The production term in the species continuity equation depends on the number densities and rate constants of the chemical reactions involved. The rate constants for the electron collision reactions depend on the electron temperature. Therefore the electron energy equation is solved to obtain T_e, the electron temperature. The transport properties of the electrons are calculated using this quantity.

$$\frac{\partial e_e}{\partial t} + \vec{\nabla}\cdot((e_e + p_e)\vec{u}_e - \kappa_e\vec{\nabla}T_e) = +e\vec{f}_e\cdot\vec{\nabla}\phi - e\sum_i \Delta E_i^e r_i + \frac{3}{2}k_Bn_e\frac{2m_e}{m_{k_b}}(T_e - T_g)\bar{\nu}_{e,k_b}$$

Here e_e represents the electron temperature given by $\frac{3}{2} n_e k_B T_e$, p_e is the electron pressure given by $n_e k_B T_e$, $\vec{u}_e \vec{u}_e$ is the electron convective velocity obtained from the drift diffusion approximation and K_e is the electron thermal conductivity. The source terms on the right hand side represent the electron joule heating term given by $e\vec{f}_e.\vec{\nabla}\phi$ $e\vec{f}_e.\overrightarrow{\nabla\phi}$, the inelastic electron collision term given by $-e\sum_i \Delta E_i^e r_i$ ($\Delta E_i^e \Delta E_i^e$ is the energy of the reaction with *i* and r_i being the rate of progress) and the elastic collision term given by

$$\frac{3}{2} k_B n_e \frac{2m_e}{m_{k_b}} (T_e - T_g) \bar{\nu}_{e,k_b}$$

where T_g is the common heavy species gas temperature, m_e represents mass of electron, m_{kb} represents mass of heavy species and $\bar{\nu}_{e,k_b}$ represents the electron background species collision frequency.

3. Gas Energy Equation

The temperature of the heavy species can be obtained from the gas temperature equation given by

$$\frac{\partial \sum_{k\in H} n_k h_{k,\text{sens}}}{\partial t} + \vec{\nabla} \cdot \left(\sum_{k\in H} \vec{f}_k h_{k,\text{sens}} - \sum_{k\in H} \kappa_k \vec{\nabla} T_g \right) = S_{T_g}$$

The summation is done over all the heavy species since they have a common gas temperature.
$h_{k,sens}$ $h_{k,sens}$ is the sensible enthalpy of heavy species *k* given by

$$h_{k,\text{sens}} = \int_0^{T_g} C_{p_k} dT \approx C_{p_k} T_g$$

The source term S_{T_g} is given by

$$S_{T_g} = \eta_J \left(-e \sum_{k\in H} Z_k \vec{f}_k . \vec{\nabla}\phi \right) - \frac{3}{2} k_B n_e \frac{2m_e}{m_{k_b}} (T_e - T_g) \bar{\nu}_{e,k_b} - \sum_{k\in H} \dot{G}_k (\Delta h_f)_k^0$$

The first term on the right hand side is the ion joule heating, the second term is the energy gained or lost due to elastic collisions with electrons and the last term represents the energy gained or lost due to inelastic collisions.

4. Electrostatic Poisson Equation

The potential ϕ used in the drift diffusion approximation is obtained from the Electrostatic Poisson equation given by

$$\nabla^2 \phi = -\frac{e}{\varepsilon_0} \sum_k Z_k n_k$$

Here Z_k represents the charge number on the species k, e is the electronic charge and n_k represents the number density of species *k*.

5. Plasma Chemistry

The neon nitrogen chemistry used in the plasma model involves four neon species, Ne, Ne^+, Ne_2^+, Ne*, electrons, and four nitrogen species, viz N_2, N, N^+ and N_2^+. Ne* represents the metastable neon species. The reaction rate constants of the neutral ionization and excitation reactions are obtained by finding the energy distribution functions of electrons using the Boltzmann Equation solver BOLSIG+.[16]

Table 3. Neon/nitrogen chemistry[20]

	reactions	Rate constant (cm, s, #)	ΔE(eV)	Ref
G1	$2e + N_2^+ \rightarrow N_2 + e$	$5.651e(-27)\ T_e^{-0.8}$	-15.6	17
G2	$e + N_2^+ \rightarrow N + N$	$2.54e(-6)\ T_e^{-0.5}$	-5.8	17
G3	$e + N_2 \rightarrow N + N + e$	$1.959e(-6)\ T_e^{-0.7}\ \exp(1.132e(5) / T_e)$	9.757	17

G4	$e + N \rightarrow N^+ + 2e$	$8.401e(-5) \exp(-1.682e(5) / T_e)$	14.50	17
G5	$e + N_2 \rightarrow N_2^+ + 2e$	$4.483e(-7)\ T_e^{-0.3} \exp(-1.81e(5) / T_e)$	15.6	17
G6	$e + N_2 \rightarrow e + N_2$	BOLSIG+	1	20
G7	$Ne^* + N_2 \rightarrow Ne + N_2^+ + e$	7.0e(-11)	-0.6	17
G8	$Ne^+ + N_2 \rightarrow Ne + N^+ + N$	7.0e(-10)	2.74	17
G9	$Ne^+ + N_2 \rightarrow Ne + N_2^+$	5.0e(-10)	-6.0	17
G10	$Ne_2^+ + N_2 \rightarrow 2Ne + N_2^+$	5.0e(-10)	-6.0	17
G11	$Ne_2^+ + N_2 \rightarrow 2Ne + N^+ + N$	7.0e(-10)	2.74	17
G12	Ne + e → Ne+ + 2e	BOLSIG+	21.56	17
G13	Ne + e → Ne* + e	BOLSIG+	16.62	17
G14	Ne* + e → Ne+ + 2e	$4.1e-8\ Te^{0.74} \exp(-58022.5/T_e)$	4.90	18
G15	Ne+ + 2Ne → Ne2+ + Ne	4.4(e-32)		19
G16	Ne2+ + e → Ne* + Ne	$3.7(e-8)\ Te^{(-0.43)}$		19
G17	2Ne* → Ne + Ne+ + e	3.2e(-10)		19

The reaction G6 does not represent an elastic collision of N_2 with an electron. It represents a series of excitation and dexcitation reactions of vibrational excited states of Nitrogen. Information about how the rate constants and energies for these reactions are calculated as given in Ref. 20.

6. Transport Properties

The species mobility of ions and electrons are obtained as

$$\mu_k = \frac{eZ_k}{m\bar{\nu}_{k,k_b}}$$

Where Z_k is the charge number of species k, m the mass of background neutral species and $\bar{\nu}_{k,k_b}$ is the collision frequency of species k with the neutrals.

The species diffusion coefficient D_k which appears in the drift diffusion approximation is given by Einstein's relation

$$D_k = \frac{k_B T_k}{eZ_k}\mu_k$$

where T_k is the temperature of species k.

7. Bulk Flow Equations

The compressible Navier-Stokes Equations are used to find the bulk velocity and gas temperature which will go as input for the plasma solver. The equations are solved on a 2D axi-symmetric unstructured cell centered finite volume framework. The two dimensional form of the compressible Navier-Stokes equation is given by

$$\frac{d\mathbf{U}}{dt} + \vec{\nabla}\cdot\vec{\mathbf{F}}_{inviscid} = \vec{\nabla}\cdot\vec{\mathbf{F}}_{visc} + \mathbf{S}$$

Here U represents the four conservative variables ($\rho, \rho V_x, \rho V_r, \rho e_t$) where ρ is the density, $\boldsymbol{V_x}$ the axial velocity, V_r the radial velocity and e_t represents the total internal energy.

$\vec{\mathbf{F}}_{inviscid}$ represents the inviscid flux term, $\vec{\mathbf{F}}_{visc}$ represents the viscous flux term, and S represents the source term which is obtained from the plasma solver.

These equations are solved using a dual time stepping algorithm. The electrostatic forces and collisions contribute to the momentum source term which is obtained from the plasma solver given by

$$\vec{f} = \sum_i n_i(\vec{u}_i - \vec{V})\bar{\nu}_{i,k_b} - \frac{e n_e \vec{E}}{m_e}$$

The source term for the energy equation is given by

$$S_{Heat} = -\alpha_J (e\sum_h Z_k \vec{f}_k \cdot \vec{\nabla}\phi) + \frac{3}{2} k_B n_e \frac{2m_e}{m_{k_b}} (T_e - T_g)\bar{\nu}_{e,k_b} - e\sum_{j=1}^{I_g} \Delta E_j^g r_j$$

The first term in the energy source term is the Ion Joule heating, the second term is the contribution of elastic collision of heavy species with electrons and the last term represents the inelastic collision term of heavy body species with electrons.

B. Computational Results

The hybrid unstructured mesh used for the simulation is shown in Fig. 11. First the cold gas flow is solved to steady state to obtain the pressure, temperature and density distribution inside the thruster. These act as the input for the plasma solver.

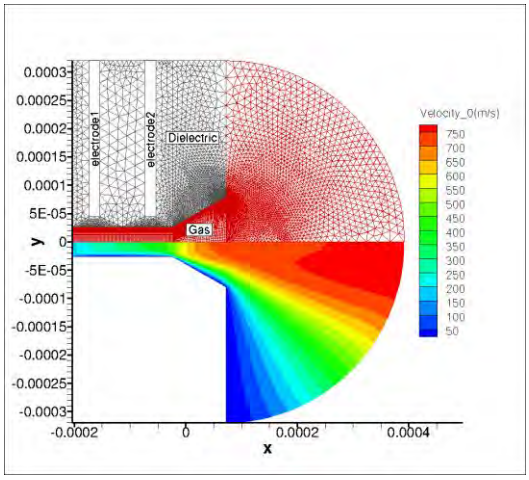

Figure 11. Computational mesh and axial velocity distribution.

The total pressure (1 atm) and temperature (300 K) act as the boundary condition at the inflow subsonic section. A very low exit pressure of 10 Pa is enforced at the exit. The dielectric walls of the thruster are assumed to be viscous at a fixed temperature of 300 K. The cold gas flow is solved to steady state. The contour plot of the axial velocity is shown in Fig.11.

After the flow has run to steady state, the plasma is switched on. An oscillating voltage with a peak of 1500 V and 50 kHz is applied at the upstream electrode while the downstream electrode is grounded. The dielectric walls are assumed to have a solid surface flux of ions and electrons. The flux of ions is obtained from the Maxwellian flux on the wall. The electron flux on the wall will include secondary electron emission as well.

Figures 12 and 13 show a dielectric barrier discharge where the plasma is pulsed. For every half cycle of the ac voltage we see a current pulse where the breakdown happens. During the positive half cycle when the voltage increases sinusoidally, breakdown of the gas happens. Charge trapping occurs due to an electric field which is induced in the opposite direction as the applied electric field. This quenches the plasma completely and the particle current through the plasma comes back to zero. During the negative half cycle, the induced electric field supplements the applied electric field and brings about another breakdown. The plasma is subsequently quenched after charge trapping. The width of the pulse is about 0.1 μs which is 10 times smaller than the flow time scale.

Figures 12 and 13 also show the increase in the electron and Ne* number density at five instances during the growth of the pulse respectively. The time interval between each snapshot is 10 ns. The electrons are generated close to the powered electrode. The peak number densities move towards the grounded electrode over time in the direction

of flow. The metastable neon species also show a similar trend except for the burn out at the centre due to stepwise ionization. Peak electron densities exceeding 10^{20} m^{-3} are observed. Peak pulse conditions are reached 50 ns from the initiation of the pulse with total duration of about 0.1 μs.

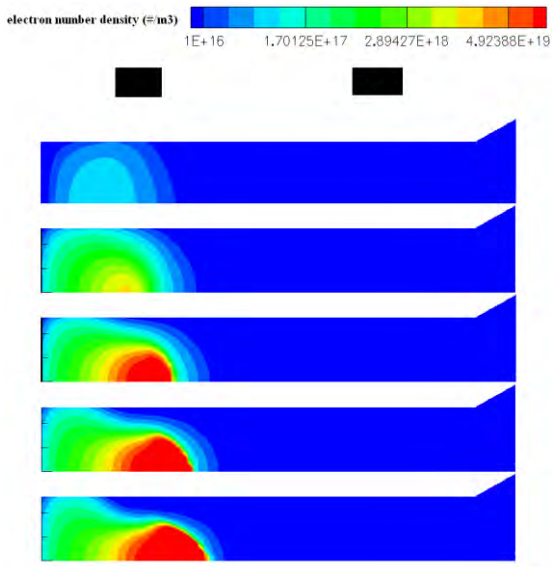

Figure 12. Electron number density during onset of the pulse.

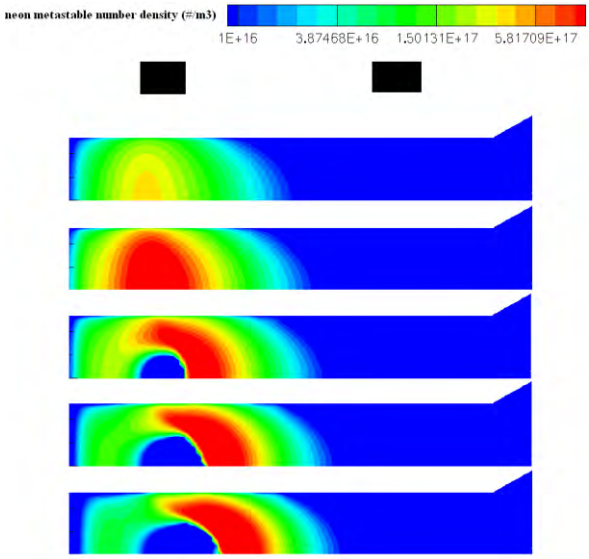

Figure 13. Neon metastable number density during onset of the pulse

V. Future Work

Future efforts will focus on increasing the discharge temperature and nozzle efficiency. Increasing both of these factors will yield substantial thrust gains and further increase the viability of the MCD thruster as a means of satellite propulsion.

VI. Summary

Initial experimental and computational research has been performed on the MCD thruster. Low power heating tests on a 110 μm diameter Al/Al_2O_3 microcavity with a choked flow of a Ne + N_2 mixture indicate that a low fraction of the electrical power is lost to the wall. Separate thrust stand tests on a microcavity with an integral but non-optimum nozzle give thrust coefficients consistent with supersonic flow at the Reynolds numbers tested.

Acknowledgments

This research has been supported by the United States Air Force Office of Scientific Research grant #AF FA9550-09-1-0161. Student support has been provided by NASA Space grant #NNG05GE81H and NSF grant #EEC-06 48996.

References

[1]Eden, J. G., Park, S. –J., Ostrom, N. P., Chen, K. -F., Kim, K. S. "Large Arrays of Microcavity Plasma Devices for Active Displays and Backlighting." *IEE/OSA Journal of Display Technology*, Vol. 1, No. 1, Sept. 2005, pp. 112-116.

[2] Park, S.-J., Kim, K. S., Eden, J. G. "Nanoporous Alumina as a Dielectric for Microcavity Plasma Devices: Multilayer Al/Al_20_3 Structures." *Applied Physics Letters*, Vol. 86, No. 22, 2005 pp. 1-3.

[3] Seo, J. H. and Eden, J. G., "Two-Dimensional Simulation of AC-Driven Microplasmas Confined to 100-300 μm Diameter Cylindrical Microcavities." *Journal of Applied Physics*, Vol. 100, No. 12, 123302, Dec. 2006.

[4] Bayt, R. L., "Analysis, Fabrication and Testing of a MEMS-based Micropropulsion System." Ph.D Dissertation, Department of Aeronautics and Astronautics, MIT, Cambridge, MA 1999.

[5] Delft University of Technology, "Resistojet Configurations." 2006, URL: http://www.lr.tudelft.nl/live/pagina.jsp?id=353bb7e5-d814-4a1f-9565-6ee7e9481b06&lang=en. [cited 9 September 2009].

[6] Morren, W.Earl, Hay, Stuart S., Haag, Thomas W., Sovey, James S. "Performance Characterizations of an Engineering Model Multipropellant Resistojet." *Journal of Propulsion and Power*, Vol. 5, No. 2, Mar.-Apr. 1989 pp. 197-203.

[7] Willmes, G. F. and Burton, R. L., "The Low Power Helium Pulsed Arcjet." *Journal of Propulsion and Power*, Vol. 15, No. 3, May.-Jun. 1999 pp. 440-446.

[8] Burton, R. L. and Willmes, G., The University of Illinois, Urbana, IL U.S. "Pulsed Thruster System." U.S. Patent No. 6,295,804, Filed: Oct. 2, 2001.

[9] Takao, Y., Ono, K., "A Miniature Electrothermal Thruster Using Microwave-excited Plasmas: A Numerical Design Consideration." *Plasma Sources, Science and Technology*, Vol. 15, No. 2, May 2006 pp. 211-27.

[10] Slough, J., Andreason, S., Ziemba, T., and Ewing, J. J., "Micro-discharge Micro-thruster," AIAA Paper No. 2005-4074, Jun. 2005.

[11] Burton, R. L., Rysanek, F., Antonsen, E. A., Wilson, M. J., and Bushman, S. S., "Pulsed Plasma Thruster Performance for Microspacecraft Propulsion." *Micropropulsion for Small Spacecraft*, edited by M. Micci, Progress in Aeronautics and Astronautics, Vol. 187, AIAA, Washington DC, 2000, pp. 337 - 352.

[12] Kim, K. S., S.-J. Park, and J. G. Eden, "Self-patterned aluminum interconnects and ring electrodes for arrays of microcavity plasma devices encapsulated in Al_2O_3." J*ournal of Physics D: Applied Physics*, vol. 41, 012004, January 2008.

[13] Kim, K. S., T. L. Kim, J. K. Yoon, S.-J. Park, and J. G. Eden, "Control of cavity cross-section in microplasma devices: Luminance and temporal response of 200 × 100 and 320 × 160 arrays with parabolic Al_2O_3 microcavities." *Appl. Phys. Lett.*, vol. 94, 011503, January, 2009.

[14] Wilson, Bushman, and Burton, "A Compact Thrust Stand For Pulsed Plasma Thrusters." IEPC Paper No. 97-122, 1997.

[15] Deconinck, T., Mahadevan, S. and Raja, L. L., "Simulation of Direct-Current Microdischarge for the Micro Plasma Thruster." *IEEE Transactions on Plasma Science*, Vol. 36, No. 4, Aug 2008, pp. 1200-1201.

[16] BOLSIG+ Electron Boltzmann Equation Solver Ver. 1.1, Gerjan Hagelaar, Laboratoire Plasma et Conversion d'Energie, Université Paul Sabatier, Toulouse, France.

[17] Yuan, X. and Raja, L. L., "Computational Study of Capacitively Coupled Atmospheric-Pressure Glow Discharge in Helium." *IEEE Transactions on Plasma Science*, Vol. 31, No. 4, Aug. 2003, pp. 495-503.

[18] Levin, L. A., Moody, S. E., Klosterman, E. L., Center, R. E., Ewing, J. J., "Kinetic Model for Long-Pulse XeCl Laser Performance." *IEEE Journal of Quantum Electronics*, Vol. QE-17,No. 12,Dec 1981.

[19] Meunier, J., Belenguer, Ph. And Boeuf, J. P., "Numerical Model of an AC Plasma Display Panel Cell in Neon-Xenon Mixtures." *Journal of Applied Physics* 78 (2),15 July 1995.

[20] Deconinck, T., Mahadevan, S. and Raja, L. L., "Simulation of Direct-Current Surface Plasma Discharge Phenomena in High-Speed Flow Actuation." *IEEE Transactions on Plasma Science*, Vol. 35, No. 5, Oct 2007, pp. 1301.